

Microlensing, structure of the galactic halo and determination of dark objects’ mass function

D. Marković and J. Sommer-Larsen

Theoretical Astrophysics Center, Juliane Maries Vej 30, DK-2100 Copenhagen Ø, Denmark

12 December 1996

ABSTRACT

We study the accuracy and systematic error of inference of massive halo objects’ (MHO or ‘Macho’) mass function from microlensing events observed in the direction of Large Magellanic Cloud. Assuming the spatial distribution and kinematics of the objects are known, the slope and the range of the MHO mass function (modeled here by a simple power law) will be possible to determine from 100-1000 detected events *if* the slope is in the range $-2.5 \lesssim \alpha \lesssim -0.5$, with the statistical errors reaching their minima at $\alpha = -1.5$. Outside this range the errors grow rapidly making the inference difficult even at very large numbers of events ($N \approx 10000$). On the other hand, the *average* mass of the MHO’s will be determined to better than about 30% accuracy from $N \approx 100$ events for *any* slope. Overall, we find that the accuracy of inference at fixed N will not be strongly affected by the presently available event duration-dependent detection efficiencies if the typical MHO masses are in the range (order of magnitude $0.1M_{\odot}$) indicated by the events detected so far.

We also estimate the effects of the uncertainty of the massive objects’ spatial distribution and kinematics on the determination of their mass function. The massive objects’ halo models considered are all spherical but we allow for various density profiles and a radius-dependent, anisotropic velocity dispersion. We find that while the mass function slope and range (i.e., the ‘shape’) are weakly affected for $-2 \lesssim \alpha \lesssim 0$, the error in the average mass due to the halo structure uncertainties could be reduced to less than about 50% only through the detection of about 1000 or more events. Reliable estimates of the halo structure itself [density profile and (anisotropic) velocity dispersion profile] can start only at very large numbers of detections ($N \gtrsim 10000$).

Key words: Microlensing – Galactic halo – Macho mass function.

1 INTRODUCTION AND OVERVIEW

A decade after Paczynski’s ground-breaking proposal (1986) several teams and considerable resources around the world are now devoted to searches for microlensing events [see recent overviews by Paczynski (1996) and Roulet & Mollerah (1996)]. These searches have been rewarded by by a large number (~ 100) of detections in the direction of the galactic bulge and already a significant set of events observed [1 or 2 by the EROS team (Aubourg *et al.* 1993) and 6-8 by the MACHO team (Alcock *et al.* 1996)] along the line of sight to the Large Magellanic Cloud.

In the latter case microlensing is expected to provide us with direct information on the composition of the galactic halo. A statistical analysis (Alcock *et al.* 1996) of the presently available data suggests that dark massive objects — the potential microlenses — could account for between 30% and 100% of the total mass in the halo. In addition, their most likely masses should be in the range $0.1\text{--}0.6M_{\odot}$.

The admittedly large uncertainty stems in part from the still small number of events and thus a poor statistics, but also from our lack of knowledge [as made clear in (Alcock *et al.* 1996)] regarding the spatial distribution and kinematics of the massive halo objects (MHO). The import of the halo structure is due to the simple fact that the (inferred) mass of a lens scales as $m \sim (Tv_n)^2/D_L(D_S - D_L)$, where T is the *observed* duration of the microlensing event, v_n is the MHO’s velocity orthogonal to the line of sight, D_L is the earth-lens distance and D_S is the earth-source distance. At the same time, the integral event rate which is roughly proportional to $\int \rho \sqrt{D_L(D_S - D_L)} v_n dD_L$ obviously incorporates details about halo beyond the mere total mass $M_{\text{tot}} \sim \int \rho d^3D_L$. Therefore, the conversion from the observed quantities, the event durations and the rate, to information on MHOs’ masses and their halo’s total mass inevitably involves assumptions about the structure of the halo.

A question arises at this point: should we expect — as might seem only natural — that, given a larger num-

ber of detections in a foreseeable future, the determination of the MHO mass function and the MHOs' fraction of the total halo mass could reach a significantly higher accuracy thus providing us with better clues regarding the origin and evolution of the halo. The present paper will address this question.

Recently Mao and Paczynski (1996) studied the issue of MHOs' mass determination. By considering simplified 'toy' models (e.g., uniform spatial density of MHOs) they were able to estimate that a reliable determination of the mass function could be achieved if we had 100 or more events. They modeled the mass function by a simple power law $dn/dm \propto m^\alpha$ (as we shall do in this paper) and concluded that for $\alpha \ll -1.5$ ($\alpha \gg -1.5$) the high (low) mass end of the mass function will be difficult to probe. As they pointed out, their results depended on the assumption that the MHOs' spatial distribution and kinematics were known.

In this paper we also at first assume that the halo model is known. The specific model used in Section 4 for the purpose of mass function inference is the isothermal sphere with a core (CIS). Although the underlying halo model is considerably more realistic in our case, the basic conclusion of Mao and Paczynski remains valid: in the vicinity of $\alpha = -1.5$ the slope and range $\beta = \log_{10}(m_{\max}/m_{\min})$ can be determined with $N \gtrsim 100$ events. However, as we shift away from $\alpha = -1.5$, the error of determination grows very rapidly. In particular, for a positive slope α one needs $N > 1000$ events for a reliable inference. [It is to be hoped — perhaps not unrealistically — that the actual mass function of the MHOs will indeed correspond to α sufficiently close to -1.5 .] A quantity that can be accurately ($\lesssim 30\%$ error) inferred with $N \gtrsim 100$ at any slope is the average mass of the MHOs, i.e., the first moment of the mass function. We find that our results do not depend dramatically (see, e.g., Fig. 6) on whether the detection efficiency is flat (i.e. independent of event duration) or of the type presently available for the MACHO project's microlensing searches (Alcock *et al.* 1996).

The effects of halo structure uncertainty will receive our attention in the later part (section 5) of the paper. At the outset of section 5 we will perform the following 'experiment': we will assume that a specific spherical halo model describes the actual halo accurately enough (this model will be called the 'real' one). We will then ask what the effect on mass function and MHOs' halo fraction determination is if, instead of the 'real' model, we use for the inference a different one, the isothermal sphere (chosen here in its singular, $\rho \sim r^{-2}$, version).

For the 'real' model we take a 'concentrated' sphere (CS) with a steeper density profile, $\rho \sim r^{-3.4}$, and an anisotropic velocity dispersion. This density profile (for $r \gtrsim R_\odot$, the radius of the Sun's orbit) is commonly associated with the stellar halo (or 'spheroid') that consists of old, metal-poor stars. While the local density of the luminous halo is observed to be low $\sim 10^{-4} M_\odot/\text{pc}^3$ (Bahcall, Schmidt & Soneira 1983), it is possible that the stellar halo has a significantly more massive, dark (though plausibly baryonic) counterpart of a similar structure. [A massive, dark 'spheroid' of local density $\sim 10^{-3} M_\odot/\text{pc}^3$ was proposed in the past as a dynamically relevant component of the galaxy (Caldwell & Ostriker 1981; Rohlfs & Kreischmann 1988). Microlensing by 'spheroid' objects has

been discussed by, e.g., Giudice, Mollerach & Roulet (1994) and De Rújula *et al.* (1995).] Along with the $r^{-3.4}$ density profile, the radius-dependent velocity dispersion anisotropy (see Section 2) adopted for our CS model describes rather accurately a well known stellar halo population, the blue horizontal branch field stars, BHBFS (Sommer-Larsen, Flynn & Christensen 1994). The CS model reflects the possibility that, just like the spatial distribution of the BHBFS, the massive objects' distribution may differ from that of the total (luminous + baryonic + nonbaryonic dark matter) halo mass.

As a result of our 'experiment' we find that, although α and β are weakly affected by the halo model ambiguity, the inferred $\bar{\mu}$ is on the average about 60% greater than the real value. It is important that unless $N \gtrsim 1000$, the statistics based only on event durations does not allow us to distinguish between the two massive objects' halo structures; the differences between them are submerged in the statistical noise.

These results indicate that the uncertainty of the inferred average mass will be difficult to reduce below about the factor of 2. A similar conclusion, with similar magnitudes of relative errors, holds for the massive object halo's local density ρ_o and the total halo mass between the solar orbit and LMC, M_{tot} . The unresolvable (at $N < 1000$) ambiguity is characteristic of a broad range of halo models that one might choose as the 'real' ones instead of CS, although the ensuing uncertainty of the inferred average dark objects' mass and their total halo mass may be smaller than that obtained in the specific case of the CS/SIS ambiguity. [Since the inferred halo density in the vicinity of the Sun for the CS model is about twice the value for the isothermal sphere, it may be possible to rule out the more concentrated (e.g. $\rho \sim r^{-3.4}$ at $r \gtrsim R_\odot$) halo models on the basis of dynamical arguments even at $N \lesssim 100$ if the MHO halo indeed turns out to be very massive, i.e., approaching the total halo mass. For more detail see (Sommer-Larsen & Markovic 1997).] These results are supported by our maximum likelihood simulations presented in Section 5, where the (appropriately parametrised) halo model is treated as unknown and its parameters are varied together with the mass function parameters: only at $N \gtrsim 1000$ events do the errors in $\bar{\mu}$, ρ_o and M_{tot} fall below 50%.

Given the current detection rate of a few events per year, and even hoping that it could be increased in the future, the very large number of events needed does not support optimism regarding an accurate inference of MHOs' masses and their halo fraction on the basis of LMC events only. Probing the halo at various angles relative to the center of galaxy, e.g. through the observation of events toward M31, could help distinguish between different halo models. A considerable improvement might come from gaining more information from individual events by, e.g., parallax measurements (Refsdal 1966; Gould 1992, 1994, 1995b) that could put tight constraints on MHOs' spatial distribution and/or kinematics.

This paper is organised as follows. In Section 2 we review the halo models that will be used in the subsequent sections. Section 3 outlines the derivation of microlensing rates. In Section 4 we discuss the MHOs' mass function determination errors assuming a *known* halo model while in section 5 we study the effects of halo model uncertainties.

Finally, the Appendix provides some statements and formulae of mathematical statistics (along with the derivations) that are extensively used in the main body of the paper.

2 MODELS OF MHO DISTRIBUTION AND KINEMATICS

In this paper we will consider a range of models of the massive halo objects' distribution and velocities. For simplicity, we will restrict our discussion to spherically symmetric halos. One of the most commonly used models is the isothermal sphere with the velocity dispersion constant throughout the halo the density profile which is well approximated by

$$\rho(r) = \rho_o \frac{a^2 + R_\odot^2}{a^2 + r^2}, \quad (1)$$

where $a \approx 5$ kpc is the 'core' radius and $R_\odot = 8.5$ kpc is the distance of the Sun from the galactic centre. Assuming that the total (luminous + dark matter) halo density is distributed according to expression (1), one obtains the observed (approximately) flat rotation curve for the galaxy.

The HMO mass distribution, however, need not follow that of the total halo mass. One possibility is that the massive objects may be more concentrated toward the galactic centre. We may thus follow the clues provided by recent observations (Sommer-Larsen, Flynn & Christensen 1994) of the blue horizontal branch field stars (BHBFS) in the outer halo. These observations imply that the velocity dispersion changes from $\beta \equiv 1 - \sigma_\theta^2/\sigma_r^2 > 0$ at smaller distances from the centre of the Galaxy to $\beta < 0$ at larger distances. The radial velocity dispersion is well described by the analytic fit

$$\sigma_r^2 = \sigma_o^2 + \sigma_+^2 \left[\frac{1}{2} - \frac{1}{\pi} \tan^{-1} \left(\frac{r - r_o}{l} \right) \right], \quad (2)$$

where the best agreement with the observations is achieved with $\sigma_o = 80 \text{ km s}^{-1}$, $\sigma_+ = 145 \text{ km s}^{-1}$, $r_o = 10.5$ kpc and $l = 5.5$ kpc. The BHBFS halo is close to spherical with the density that is well modeled by the power law $\rho = \rho_o(R_\odot/r)^\gamma$, where $\gamma \approx 3.4$.

From the Jeans' equation for spherical systems (Binney & Tremaine 1987)

$$\frac{1}{\rho} \frac{d(\rho \sigma_r^2)}{dr} + \frac{2\beta \sigma_r^2}{r} = -\frac{d\Phi}{dr}, \quad (3)$$

where $\Phi(r)$ is the gravitational potential, we obtain the tangential velocity dispersion

$$\sigma_t^2 = \frac{1}{2} V_c^2 - \left(\frac{\gamma}{2} - 1 \right) \sigma_r^2 + \frac{r}{2} \frac{d\sigma_r^2}{dr}, \quad (4)$$

where $V_c = (-rd\Phi/dr)^{1/2}$ is the (roughly constant) rotation velocity. Notice that given both the negative slope of the radial velocity dispersion

$$r \frac{d\sigma_r^2}{dr} = -\frac{1}{\pi} \frac{r}{l} \frac{\sigma_+^2}{1 + [(r - r_o)/l]^2}, \quad (5)$$

and $\gamma > 2$, the tangential velocity dispersion will be smaller than in the case of an isothermal sphere ($\alpha = 2$, $\sigma_r = \text{const.}$ at large radii) with the same V_c [see Fig. 1]. This increased 'pressure support' is merely a consequence of the collisionless Boltzmann equation and — in the final instance — the conservation of the phase-space volume (Liouville's theorem).

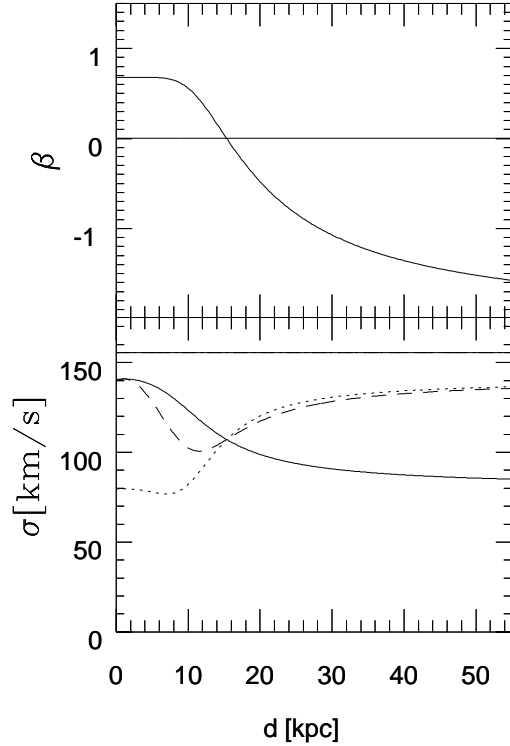


Figure 1. Anisotropy parameter β and velocity dispersion for halo model CS as functions of the distance d from the Earth in the direction of LMC; σ_r is given by the solid line, σ_t by the dotted line and σ_x [see paragraph preceding equation (11)] by the dashed line. The straight solid lines correspond to the singular isothermal sphere, SIS ($\beta = 0$, $\sigma = 156 \text{ km/s}$).

It is realistic enough — and will prove quite convenient in the following — to model the velocity distribution by the Gaussian

$$f(v_r, v_\theta, v_\phi) = \frac{1}{(2\pi)^{3/2}} \frac{1}{\sigma_r \sigma_t^2} \exp \left[-\frac{1}{2} \left(\frac{v_r^2}{\sigma_r^2} + \frac{v_\theta^2 + v_\phi^2}{\sigma_t^2} \right) \right], \quad (6)$$

where σ_r and σ_t are given by equations (2) and (4) for power-law profiles.

In this paper we will adopt the following nomenclature for models of the massive objects' halo: for the power-law halo with $\gamma = 2$ and an isotropic velocity dispersion we will use the familiar name, singular isothermal sphere ('SIS'); if the density profile has a core (1) and the velocities are still distributed according to an isotropic version of (6) with constant $\sigma_r = \sigma_t = V_c/\sqrt{2}$, we will use the shorthand 'CIS' (strictly, this model does not satisfy Jeans' equation); the massive objects' halo model corresponding to that of BHBFS with the power-law density profile $\gamma = 3.4$ and the dispersion given by (2) and Jeans' equation will be called the 'concentrated sphere' ('CS').

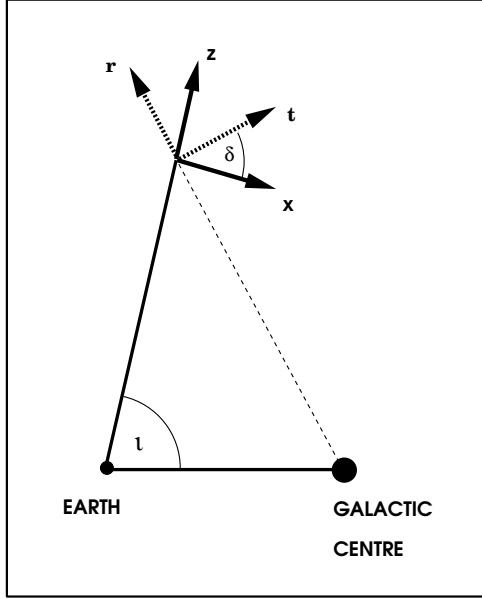


Figure 2. Coordinates and angles used in the derivation of the lensing events rate.

3 MICROLENSING STATISTICS

The magnification of an LMC star due to the crossing of a massive object near the line of sight from the earth is given by (Paczynski 1996)

$$A(t) = \frac{u^2 + 2}{u(u^2 + 4)^{1/2}}, \quad (7)$$

where

$$u = \left(\frac{b^2 + v_n^2 t^2}{R_E^2} \right)^{1/2}. \quad (8)$$

In the above equation b is the impact parameter of the massive object relative to the line of sight, v_n is object's velocity orthogonal to the line of sight and

$$R_E = \left[\frac{4Gm}{c^2} D x (1-x) \right]^{1/2} = r_E \sqrt{\mu x (1-x)} \quad (9)$$

is the Einstein radius, where D is the distance of the LMC from the earth, $x D$ ($0 < x < 1$) is the object-earth distance, $m = \mu M_\odot$ is object's mass and $r_E = 3.2 \times 10^9$ km.

We define the duration of a microlensing event as $T = R_E/v_n$. This is a *measurable* quantity; it can be obtained as soon as one knows the maximum magnification $A_{\max} = A(u = u_{\min} = b/R_E)$ and, say, the time interval between half-magnifications $A = A_{\max}/2$ [see, e.g., (De Rújula, Jetzer & Massó 1991)]. The maximum magnification and duration are the only two measurable quantities while they depend on four parameters: m, v_n, x, b . Any information on properties of the massive object halo can thus be obtained only through a statistical analysis of a sufficiently large number of events.

The statistical analysis proceeds from the rate of microlensing events based on plausible models of dark-mass halos, such as outlined in the last section. Since the differential cross section per unit distance $x D$ for a massive object

to pass the line of sight between impact parameters $R_E u$ and $R_E(u + du)$ is $2R_E du$, the rate in the more general case is given by

$$\Gamma = N_* \int_0^1 D dx \int d\mu \frac{dn}{d\mu} 2R_E \int_0^{u_{\text{th}}} du_{\min} \int f_n(v_n) v_n dv_n, \quad (10)$$

where N_* is the number of simultaneously observed stars, $dn/d\mu$ is the differential number density of the massive objects, f_n is the probability distribution of velocities orthogonal to the line of sight and u_{th} is the threshold for successful detection [the maximum amplification is required to be greater than the threshold value, $A_{\max}(u_{\min}) > A_{\max}(u_{\text{th}})$].

In equation (10) we ignore the motions of the earth and the source orthogonal to the line of sight. While enhancing the total event rate by only a few percent in the case of sources in LMC, the observer's and source's transversal motions lead to typically shorter events (Griest 1991). Although a proper analysis of the results of *actual* microlensing searches would have to take this effect into account, we will assume in this paper that the observer and the sources are stationary. This should suffice for an analysis that attempts to isolate the effects of the halo objects' mass function, spatial distribution and kinematics. A more complete treatment would not change significantly our main conclusions regarding the accuracy of the mass function inference; the considerably greater computational effort does not seem necessary at this point.

Both $f_n(v_n)$ and $dn/d\mu$ depend on the chosen model of the massive object halo. In order to describe the velocity distribution at a point at distance $x D$ along the line of sight from the earth, we introduce a local coordinate system (see Fig. 2) so that the x axis is orthogonal to the line of sight and lies in the plane given by the earth, the center of the Galaxy and LMC, while the z axis points toward LMC. The distribution function (6) can now be rewritten in terms of the velocity components v_x, v_y and v_z ,

$$f(v_x, v_y, v_z) = \frac{1}{(2\pi)^{3/2}} \frac{1}{\sigma_t \sigma_r^2} \exp \left[-\frac{1}{2} \left(\frac{v_y^2}{\sigma_t^2} + \frac{(\cos \delta v_x + \sin \delta v_z)^2}{\sigma_t^2} + \frac{(\sin \delta v_x - \cos \delta v_z)^2}{\sigma_r^2} \right) \right], \quad (11)$$

where $\sin \delta = (R_\odot/r) \sin \iota$ and $r^2 = R_\odot^2 + (x D)^2 - 2x D R_\odot \cos \iota$ ($\iota = 82^\circ$ for the LMC). The two-dimensional velocity distribution in the plane orthogonal to the line of sight is then

$$f_t(v_x, v_y) \equiv \int f(v_x, v_y, v_z) dv_z = \frac{1}{2\pi \sigma_x \sigma_t} \exp \left[-\frac{1}{2} \left(\frac{v_x^2}{\sigma_x^2} + \frac{v_y^2}{\sigma_t^2} \right) \right], \quad (12)$$

where $\sigma_x^2 = \cos^2 \delta \sigma_t^2 + \sin^2 \delta \sigma_r^2$. It is now straightforward to obtain the distribution for velocity $v_n = |\cos \phi v_x + \sin \phi v_y|$ orthogonal to the line of sight

$$f_n(v_n) = \int_0^{2\pi} f_t(v_n \cos \phi, v_n \sin \phi) v_n d\phi$$

$$\begin{aligned}
 &= \frac{1}{2\pi\sigma_x\sigma_t} \int_0^{2\pi} d\phi v_n e^{-\frac{v_n^2}{4} \left[\frac{1}{\sigma_x^2} + \frac{1}{\sigma_t^2} + \left(\frac{1}{\sigma_x^2} - \frac{1}{\sigma_t^2} \right) \cos 2\phi \right]} \\
 &= \frac{1}{\sigma_x\sigma_t} v_n I_0 \left(\left| \frac{1}{\sigma_x^2} - \frac{1}{\sigma_t^2} \right| \frac{v_n^2}{4} \right) e^{-\frac{1}{4} \left(\frac{1}{\sigma_x^2} + \frac{1}{\sigma_t^2} \right) v_n^2},
 \end{aligned} \tag{13}$$

where we have used the identity for the Bessel function of the zero'th order $2\pi I_0(x) = \int_0^{2\pi} \exp(x \cos \phi) d\phi$ (Abramowitz & Stegun 1972). Of course, for an isotropic velocity dispersion one recovers the familiar Maxwell distribution.

As we indicated in the last section, the massive object number density will be modeled either as the power law

$$n = n_o \left(\frac{R_\odot}{r} \right)^\gamma = n_o H(x), \tag{14}$$

where

$$H(x) = \left[1 + x^2 \left(\frac{D}{R_\odot} \right)^2 - 2x \frac{D}{R_\odot} \cos \iota \right]^{-\gamma/2}, \tag{15}$$

or as the modification of (15) for $\gamma = 2$ that includes a core (1). Throughout this paper we will assume that the mass function $dn_o/d\mu$ is independent of the position in the halo.

Recalling that velocity is related to the duration of a microlensing event by $v_n = R_E/T = r_E \sqrt{\mu x(1-x)}/T$, we can change the variable of integration in (10) from v_n to T and thus obtain the rate of event *detection*

$$\Gamma = 2N_* Dr_E^3 u_{th} \int d\mu \frac{dn_o}{d\mu} \int dT \varepsilon(T) F(\mu/T^2), \tag{16}$$

where

$$\begin{aligned}
 F(\mu/T^2) &= \left(\frac{\mu}{T^2} \right)^{3/2} \int_0^1 [x(1-x)]^{3/2} H(x) \\
 &\quad \times f_n \left[r_E \sqrt{x(1-x)\mu/T^2} \right] dx.
 \end{aligned} \tag{17}$$

In the last expression we have introduced the detection efficiency $\varepsilon(T)$, i.e. the fraction of all events of duration T and satisfying $u < u_{th}$ that will be detected with the available techniques. In this paper we will use the following approximate expression for the detection efficiency

$$\varepsilon(T) = \begin{cases} 0.3 e^{-(\ln(T/T_m))^{2.6}/2.54}, & T > T_m \\ 0.3 e^{-|\ln(T/T_m)|^{1.9}/3.56}, & T < T_m \end{cases} \tag{18}$$

where $T_m = 75$ days. This expression is in good numerical agreement with the efficiency quoted by the MACHO team (Alcock *et al.* 1996) for their two-year LMC microlensing detection results.

As a model for the massive objects' mass function we choose a simple power law [see e.g. (Mao & Paczynski 1996)]

$$p_\mu(\mu) d\mu = \frac{1}{C_\beta(\alpha)} \frac{\mu^\alpha}{\mu_o^{\alpha+1}} d\mu, \tag{19}$$

for the probability that the mass of a star lies in the interval $M_\odot d\mu$. In the simplest possible case the mass function is specified, apart from the exponent α , by the range of masses $\beta \equiv \log_{10}(\mu_{\max}/\mu_{\min})$, where μ_{\max} and μ_{\min} are the upper and lower limits of the range, and by the geometric mean

$\mu_o = (\mu_{\max}\mu_{\min})^{1/2}$. The normalisation constant in equation (19) is then given by

$$C_\beta(\alpha) = \begin{cases} \beta \ln 10 & \alpha = -1, \\ \frac{1}{\alpha+1} [10^{\beta(\alpha+1)/2} - 10^{-\beta(\alpha+1)/2}] & \alpha \neq -1, \end{cases} \tag{20}$$

while the massive objects' mass density near the Sun is related to their number density by $\rho_o = n_o \mu_o M_\odot C_\beta(\alpha + 1)/C_\beta(\alpha)$.

4 DETERMINING MHO MASS FUNCTION: FIXED HALO MODEL

Given a sufficient number of detected microlensing events, one can attempt to infer the mass function of the lensing massive objects. In this section we will estimate the accuracy of such an inference. In different words, we will try to estimate just what is the 'sufficient' number of events for a reliable mass function determination.

In this section we make the important assumption that the halo structure, given by MHO's density profile and kinematics, is known (the consequences of the halo uncertainty will be discussed in the next section). We then simulate the inference of the mass function parameters μ_o , α and β from samples of a fixed number N of microlensing events of durations T_i , $i = 1, N$. We use the maximum likelihood method [for an alternative method of mass function inference, based on mass momenta see (De Rújula, Jetzer & Massó 1991; Jetzer & Massó 1994; Jetzer 1996)], where we maximise the function

$$l(\{T_i\}|\mu_o, \alpha, \beta) = \sum_{i=1}^N \ln P(T_i|\mu_o, \alpha, \beta) \tag{21}$$

with respect to the parameters μ_o , α and β [see (Gould 1995a) for a different yet equivalent formulation of the method]; we denote the values of parameters at the maximum of l by $\hat{\mu}_o$, $\hat{\alpha}$ and $\hat{\beta}$. In equation (21) $P(T|\mu_o, \alpha, \beta)$ is the normalised ($\int P(T|\dots) dT = 1$) differential event rate, $P(T) \propto d\Gamma/dT$.

Given the power-law model of the MHO mass function (20), the rate Γ [see equation (16)] can be rewritten as

$$\begin{aligned}
 \Gamma &= 2N_* Dr_E^3 u_{th} n_o \int dT \\
 &\quad \times \frac{\varepsilon(T) T^{2(\alpha+1)}}{C_\beta(\alpha) \mu_o^{\alpha+1}} \int_{\mu_o \frac{10^{-\beta/2}}{T^2}}^{\mu_o \frac{10^{\beta/2}}{T^2}} y^\alpha F(y) dy,
 \end{aligned} \tag{22}$$

where $y \equiv \mu/T^2$.

In both panels of Fig. 3 we have assumed that the MHO distribution and kinematics are well described by the isothermal sphere with a core [CIS, see equations (1) and (6)] and that we use just this (the 'real') halo model for the MHO mass function inference. The underlying ('real') mass function in the left-hand panel is given by $\mu_o = 0.86$, $\alpha = -2$ and $\beta = 2$, while that in the right-hand panel corresponds to $\mu_o = 0.06$, $\alpha = 1$ and $\beta = 2$. (The average mass in both cases is $\bar{\mu} = 0.4$.) The left columns of each of the two panels show results for $\varepsilon(T) = \text{const.}$, while in the right-hand side columns the detection efficiency is assumed to be of the form (18).

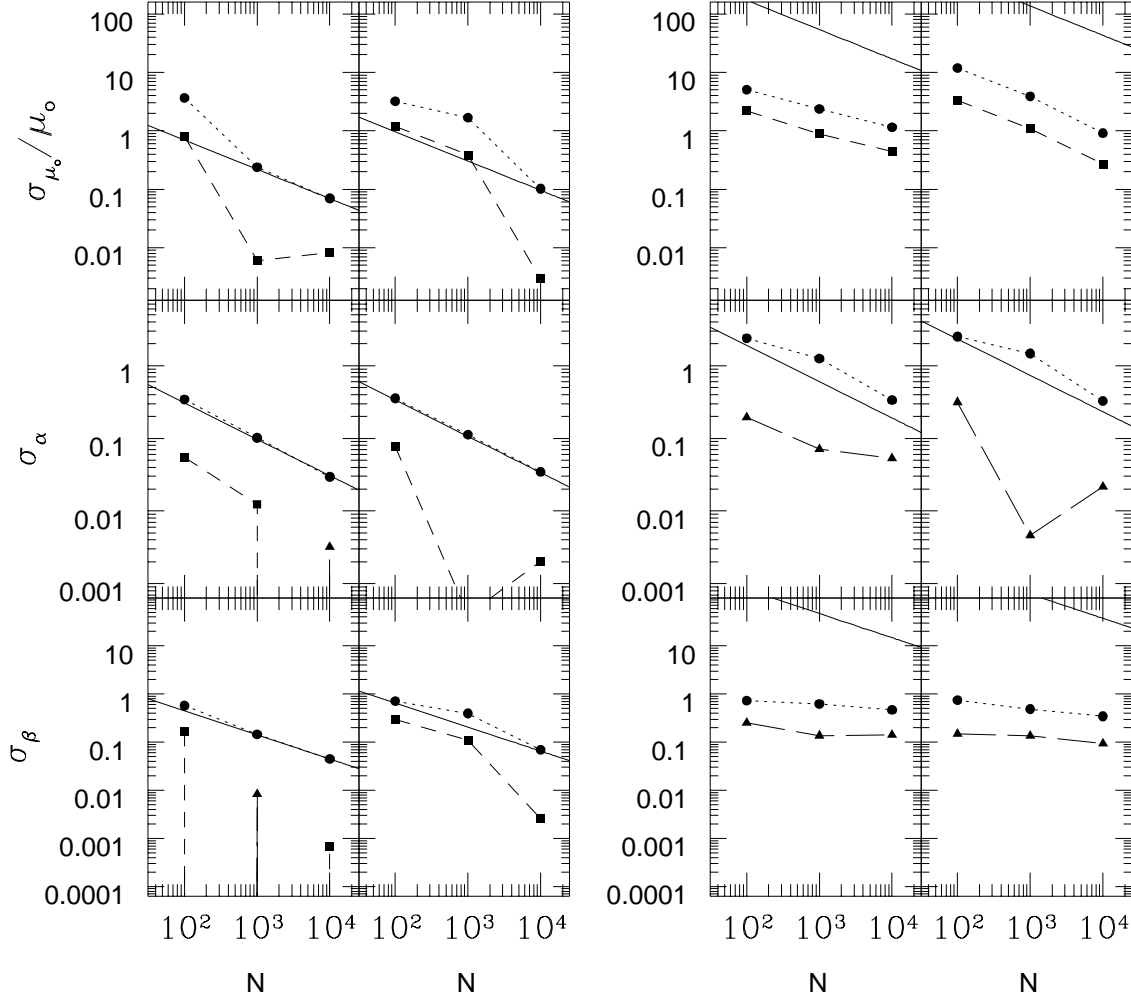


Figure 3. Dependence of variances σ_{μ_o} , σ_α and σ_β on the number of detected events for $\mu_o = 0.86$, $\alpha = -2$ and $\beta = 2$ (left panel) and $\mu_o = 0.06$, $\alpha = 1$ and $\beta = 2$ (right panel). [In both cases the average mass $\bar{\mu} = 0.4$.] In each panel the left column is based on a flat ($\varepsilon = \text{const.}$) detection efficiency, while the right-hand column assumes the MACHO-type efficiency (18). The solid circles connected by dotted lines represent the variances as obtained by Monte-Carlo simulations. The mean shift of the Monte-Carlo inferred values relative to the ‘real’ parameters (bias) is given by squares connected by short-dashed lines (positive bias) or triangles connected by long-dashed lines (absolute value of negative bias). The variances in the Cramer limit are given by solid lines.

In the figure we compare results of Monte-Carlo simulations (root-mean-square variations from the mean values of the inferred parameters are given by solid circles connected by dotted lines) for $N = 100, 1000$ and 10000 with the error estimates obtained in the so called Cramer limit (solid lines). The Cramer limit error $\sigma^c(c_\mu)$ in the determination of parameter c_μ from N data points is given by

$$[\sigma^c(c_\mu)]^2 = [I_{\mu\mu}^{(N)}(\mathbf{c})]^{-1}, \quad (23)$$

where the expression on the right-hand side is the $\mu\mu$ ’th component of the inverse of the information matrix [see Appendix, equation (A9)]

$$I_{\mu\nu}^{(N)}(\mathbf{c}) = N \int \left(\frac{\partial}{\partial c_\mu} \ln P(T|\mathbf{c}) \right) \left(\frac{\partial}{\partial c_\nu} \ln P(T|\mathbf{c}) \right)$$

$$\times P(T|\mathbf{c}) dT, \quad (24)$$

where \mathbf{c} denotes the three parameters μ_o , α and β .

For the negative slope ($\alpha = -2$) the errors in α and β are rather small at $N > 100$ and, not surprisingly, the Cramer limit is in good agreement with the results of Monte-Carlo simulations. As for μ_o , a respectable accuracy can be achieved only for $N \gtrsim 1000$ if ε is flat or for even a larger number of events if the detection efficiency is of the MACHO type. Notice, however, that convolution with a MACHO-type $\varepsilon(T)$ typically results in a relatively moderate error increase at a fixed number N of detected events. Still, the parameter estimation would take considerably more observation time due to the simple fact that this detection effi-

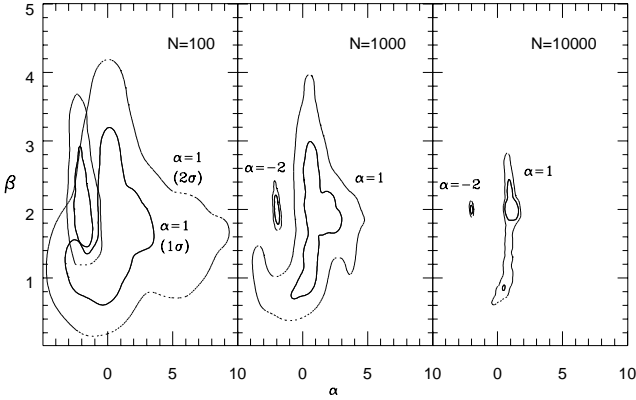


Figure 4. ‘1 σ ’ (68% confidence level) and ‘2 σ ’ (95% confidence) contours obtained by Monte-Carlo simulations of α and β inference for both $\alpha = -2$ and $\alpha = 1$. The third parameter, μ_o , has been ‘integrated’ over. The panels show results for (left to right) 100, 1000 and 10000 events. In all cases $\beta = 2$, $\bar{\mu} = 0.4$ and $\varepsilon(T) = \text{const}$. Notice the smaller size and more rapid shrinking with increasing N in the case of the contours centered on $\alpha = -2$, $\beta = 2$. At $N = 1000$ and especially at $N = 10000$ the contours are tightly concentrated around the ‘true’ value $\alpha = -2$.

ciency allows us to detect only 1/4 to 1/3 of all microlensing events, given the mass range discussed in this paper.

The errors are much larger in the positive slope ($\alpha = 1$) case. The determination of the slope itself is rather inaccurate, $\sigma_\alpha/|\alpha| > 1$, unless N approaches 10000 (see the Monte-Carlo results). Although only moderately large ($\sigma_\beta \approx 1$) at small numbers of events ($N \approx 100$), the uncertainty of β decreases very slowly for larger N . In addition, the statistical error in μ_o is hopelessly large even for the largest number of events considered in Fig. 3 (notice that $\mu_o = 0.06$).

The rather grim prospects for the inference of the $\alpha = 1$ mass function are further illustrated by the contour plots of Fig. 4. Closely related to the large errors, in about 30% of the Monte-Carlo simulations at 100 events, the maximum likelihood procedure results in a delta-function best fit for the MHO mass distribution. [This fraction falls to 2-3% at $N=1000$, and then to 0% at $N=10000$.] This is indicated by either the inferred α tending to $+\infty$ or (much less frequently) β approaching 0. In other words, the statistical errors are so large as to have a good chance of concentrating events’ duration scatter to what may look like an effect of a single-mass MHO population. These cases were excluded when the statistics of Monte-Carlo results was computed.

The irregular shape and great extent of the contours explains why Cramer limit is such a poor approximation in this case. Indeed, the Cramer limit depends only on the properties (more specifically, the first derivatives with respect to the parameters \mathbf{c}) of the distribution function in the immediate vicinity of the ‘real’ parameters. In the $\alpha = 1$ case the Cramer limit gives large errors indicating that the function is very insensitive to small changes in the parameters. However, once we shift away from the original parameters, the nonlinear distortions of the distribution function are probed and this may result in *smaller* deviations of the inferred parameters than one would expect on the basis of the Cramer

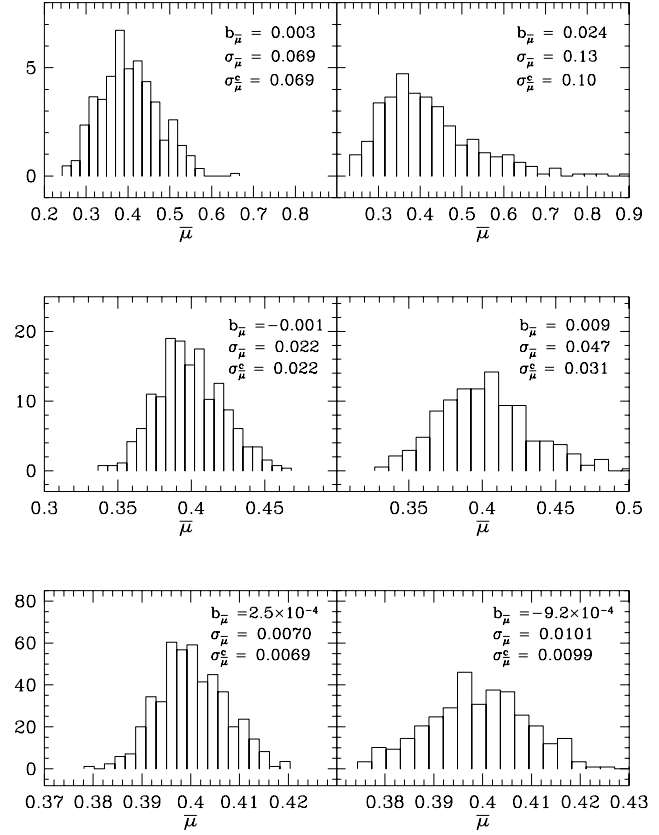


Figure 5. Histograms of inferred average masses $\bar{\mu}$ obtained by Monte Carlo simulations for the ‘real’ parameters $\mu_o = 0.86$, $\alpha = -2$ and $\beta = 2$ (thus $\bar{\mu} = 0.4$) in the case of uniform sensitivity (left) and the MACHO-type sensitivity [equation (18)] (right) for $N = 100$ (top), 1000 (middle) and 10000 (bottom) events. The numbers in the upper right corners indicate mean shifts (b) of the inferred parameters relative to the ‘real’ values, root-mean-square variances (σ) with respect to the means and the Cramer-limit errors (σ^c). The underlying halo model is the isothermal sphere with a core (CIS).

limit estimates. [This is indeed the case for μ_o and β at $\alpha = 1$ (see again Fig. 3; the Cramer limit is given by the solid lines).] Since the distribution function $P(T|\mathbf{c})$ is intrinsically so little dependent on small changes in the parameters \mathbf{c} , convolving with a MACHO-type detection efficiency $\varepsilon(T)$ will not change the estimation accuracy significantly, as can also be concluded from Fig. 3.

The very large errors in the estimation of μ_o both for $\alpha = -2$ and (especially) $\alpha = 1$ prompt us to seek a combination of the three parameters μ_o , α and β that can be inferred with greater accuracy. Not surprisingly, the average mass $\bar{\mu}$ (the first moment of the MHO mass distribution) is just such a quantity. In Fig. 5 we plot the histograms of inferred $\bar{\mu}$ for the negative slope ($\alpha = -2$) case obtained by the same Monte-Carlo simulations (400 simulations for each set of parameters, as is sufficient to obtain a relatively smooth distribution of points in the α - β plane) whose results were shown in Figs. 3 and 4. We can see that even for $N = 100$ events the average mass can be inferred with decent accuracy. Notice that the Cramer-limit errors are in good agreement with the Monte-Carlo results. The same conclu-

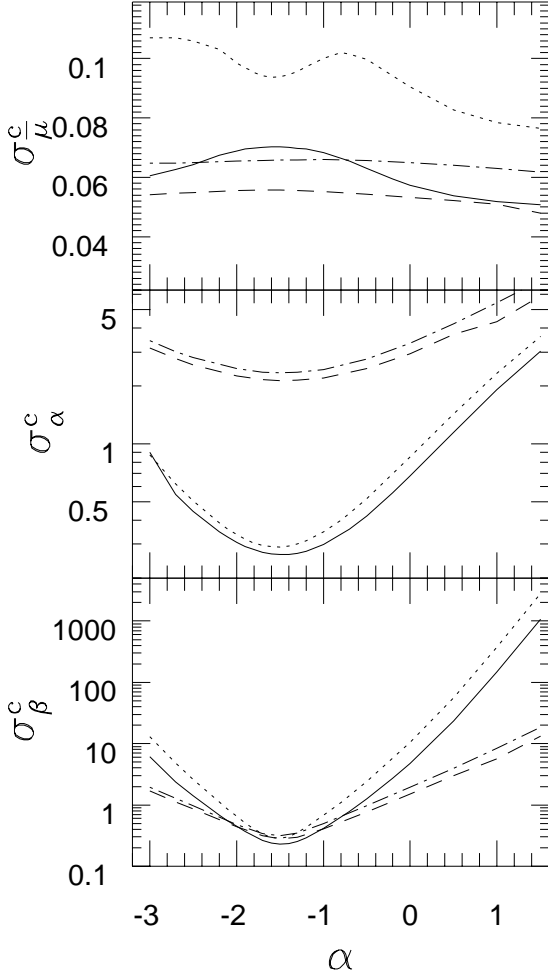


Figure 6. The dependence of the Cramer-limit errors on α . The errors (normalised to 100 events) for a ‘broad’ range, $\beta = 2$, mass function are shown as the solid [$\varepsilon(T) = \text{const.}$] and dotted [MACHO-type detection efficiency, $\varepsilon(T) \neq \text{const.}$] lines. For a ‘narrow’ mass range, $\beta = 1$, the errors are shown as the dashed and dot-dashed lines for the respective detection efficiencies.

sion — as well as similar values of the errors — holds for the positive slope $\alpha = 1$.

As we could see in Fig. 3, Cramer limit gives a poor estimate of the actual maximum-likelihood errors when those errors are large. However, if in some regions of the parameter space we detect peculiarly large Cramer-limit errors, that implies (as we have seen above) a low sensitivity of the distribution function $P(T|\mathbf{c})$ to small shifts in the underlying parameters and correspondingly indicates larger maximum-likelihood errors. By contrast, if the Cramer-limit errors are small they can indeed be used as realistic estimates of the actual inference uncertainties.

In Fig. 6 we show Cramer-limit errors, normalised to 100 events as functions of the ‘real’ α . The ‘real’ β is chosen to be 2 (‘broad’ MHO mass function) or 1. Apart from the larger errors for the MACHO-type $\varepsilon(T)$ compared to the flat ε errors, another easily predictable feature is the much poorer accuracy of the slope α determination for a narrow-range

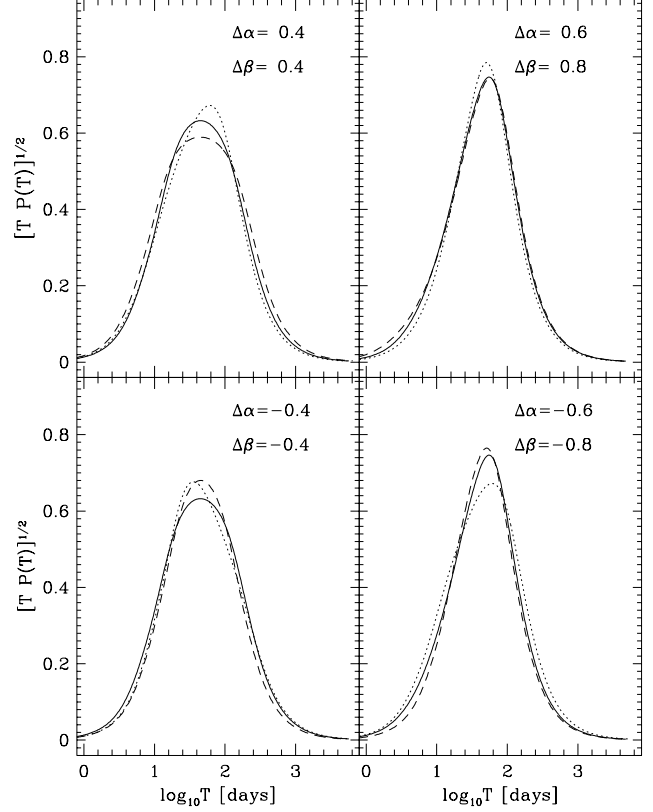


Figure 7. Changes in curves $[TP(T)]^{1/2}$ resulting from small shifts in α (dotted) and β (dashed) for $\alpha = -3/2$ (left) and $\beta = -1/2$ (right). The values of parameter shifts are indicated in the figure. The reference curves (solid lines) are chosen to have $\beta = 2$. Notice that we had to choose larger magnitudes of parameter shifts in order to produce discernible changes for $\alpha = -1/2$. $\varepsilon(T) = \text{const.}$ is assumed.

($\beta = 1$) mass function in comparison with the broad-range function: the slope is sampled much better in the latter case.

Somewhat less obvious is that the accuracy of shape (slope α and range β) determination should peak as sharply at $\alpha = -1.5$ as we observe in Fig. 6. Indeed, one would expect large uncertainties in the slope and range determination if the slope α is of large magnitude — positive or negative — thus bringing the mass distribution close to the delta function limit. The fact that the transition region between the two extremes is centered on $\alpha = -1.5$ can be understood as follows.

For large values of β expression $TP(T)$ as a function of $\ln T$ has a broad plateau [$d(TP(T))/d \ln T \approx 0$] for $\alpha = -3/2$ as can be seen from equation (22): since $F(y) \sim y^2$ for $y \ll (\sigma/r_E)^2/\bar{\mu}$ and $F(y) \sim 1/y$ for $y \gg (\sigma/r_E)^2/\bar{\mu}$ (σ is typical velocity dispersion), the last integral depends relatively weakly on T for $10^{-\beta/4} \bar{\mu}^{1/2} r_E/\sigma < T < 10^{\beta/4} \bar{\mu}^{1/2} r_E/\sigma$. Since the components of the information matrix (24) can be viewed as scalar products of the derivatives $\left(\sqrt{TP(T)}\right)_{,\mu}$ (where $\ln T$ is used as the measure), larger distortions of $\sqrt{TP(T)}$ resulting from small changes in the underlying parameters will lead to smaller errors of parameter determina-

tion. This is illustrated in Fig. 7 where we show the curves $[TP(T)]^{1/2}$ for β in the vicinity of 2 and mass function slope near $\alpha = -3/2$ (upper and lower left) and $\alpha = -1/2$ (upper and lower right). The dotted ($\Delta\beta = 0$) and dashed ($\Delta\alpha = 0$) curves show the distortions resulting from shifts in the parameters as indicated in the figure. Although β is not large, and accordingly, the ‘plateau’ is not very broad, one can clearly recognise the effects of α being equal to $-3/2$: it is due to the relatively large spread in $\ln T$ (plateau) that the curve is so sensitive to small parameter changes. In addition, the consequences of the shifts in α and β can be clearly distinguished. Thus for $\Delta\alpha = 0.3$, the mode of the curve shifts towards longer times; the rough symmetry of $\sqrt{TP(T)}$ at the plateau is broken and now longer events dominate. By contrast, the change in β only suppresses ($\Delta\beta > 0$) or sharpens ($\Delta\beta < 0$) the curve without shifting its mode. On the other hand, for $\alpha = -1/2$ a positive shift in α is closer to producing effect similar to that of a negative $\Delta\beta$. This degeneracy gives rise to a small value of the determinant of the information matrix $I_{\mu\nu}$ which enhances the errors in α and β .

The flatness of $\sqrt{TP(T)}$ in the vicinity of $\alpha = -3/2$ corresponds to roughly equal contribution of the MHO’s with masses $\mu > \mu_o$ and the ones with $\mu < \mu_o$ [see also (Mao & Paczynski 1996)] to the total event rate. As we move toward larger α , the rate is dominated by larger masses (or, if we reduce α , by smaller masses). This simple fact helps explain an interesting feature of the bottom panel of Fig. 6: while at $\alpha = -3/2$ the error in β is slightly lower for $\beta = 2$ than for $\beta = 1$ (see argument above: the plateau is broader for $\beta = 2$), this error increases more rapidly for $\beta = 2$ as we shift away from $\alpha = -3/2$. This is a consequence of the ‘tail’ (in terms of contribution to the event rate) of the mass function being less accessible [i.e. more distant from the (effective) concentration of masses at the opposite end] in the case of the larger β .

5 EFFECTS OF THE UNCERTAINTY OF MHOS’ SPATIAL DISTRIBUTION AND KINEMATICS

In this section we will study the extent to which the inference of the MHO mass function will be hampered by the unavoidable uncertainty of the massive objects’ halo structure, i.e. their distribution and kinematics. For simplicity, we will consider only spherically symmetric halos.

At first, we will estimate how much the inferred parameters of the mass function could be offset *systematically* relative to the real values if instead of fitting the event duration distribution function $P_o(T)$ based on the ‘true’ halo, we use the distribution function $P(T)$ based on a ‘false’ halo model. As we explain in the Appendix, a reasonable estimate of this shift in the parameters can be obtained by finding the mass function parameters \mathbf{c} for which the expression

$$\Psi(\mathbf{c}|\mathbf{c}_o) \equiv \int P_o(T|\mathbf{c}_o) \ln P(T|\mathbf{c}) dT \quad (25)$$

is maximised (\mathbf{c}_o denotes the ‘real’ mass function parameters).

In Fig. 8 we show distributions $P_o(T)$ based on the ‘concentrated sphere’ (CS) halo model *along with* their best

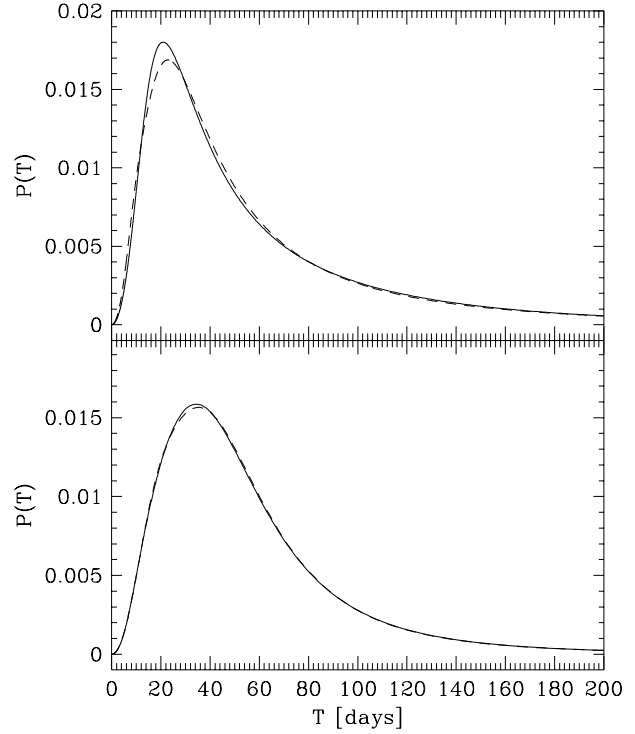


Figure 8. The differential event rate (upper panel) for $\bar{\mu}_o = 0.4$, $\alpha_o = -2$, $\beta_o = 2$ and the ‘real’ halo given by the ‘CS’ model (dashed line) and its closest SIS match ($\bar{\mu} = 0.630$, $\alpha = -1.874$, $\beta = 2.035$) [solid line] obtained by maximising (25). In the lower panel, $\bar{\mu}_o = 0.4$, $\alpha_o = 1$, $\beta_o = 2$, while the SIS-based best fit is $\bar{\mu} = 0.624$, $\alpha = -0.188$ and, $\beta = 1.415$. The two curves in the latter case are virtually indistinguishable.

matches from among the distributions $P(T)$ based on the SIS model for parameters indicated in the figure caption. [Here as throughout this section we use $\varepsilon(T) = \text{const.}$] While the two curves in the upper panel are close to each other, the ones in the lower panel are virtually indistinguishable. This is a typical situation for a broad range of the (‘real’) mass function parameters: by shifting the mass function parameters we can mask to a great extent the effects of changes in the halo model. Conversely, as long as we lack *independent* information about the MHOS’ distribution and kinematics, there always will be significant errors in the determination of the mass function from event durations only. The relatively less accurate match of the two curves in the upper panel is characteristic of the values of α that allow an accurate inference of the mass function according to the results of the last section. We will discuss below in this section how we can take advantage of this residual difference to obtain a more accurate measure of the mass function. At present we will assume that we are indeed in error regarding the MHO distribution and kinematics and are thus using a false (SIS) halo model instead of the right (CS) one. What are the magnitudes of the systematic errors that ensue?

In Fig. 9 we can observe the dependence of the systematic shift, described above, on the value of α_o for $\beta_o = 1$

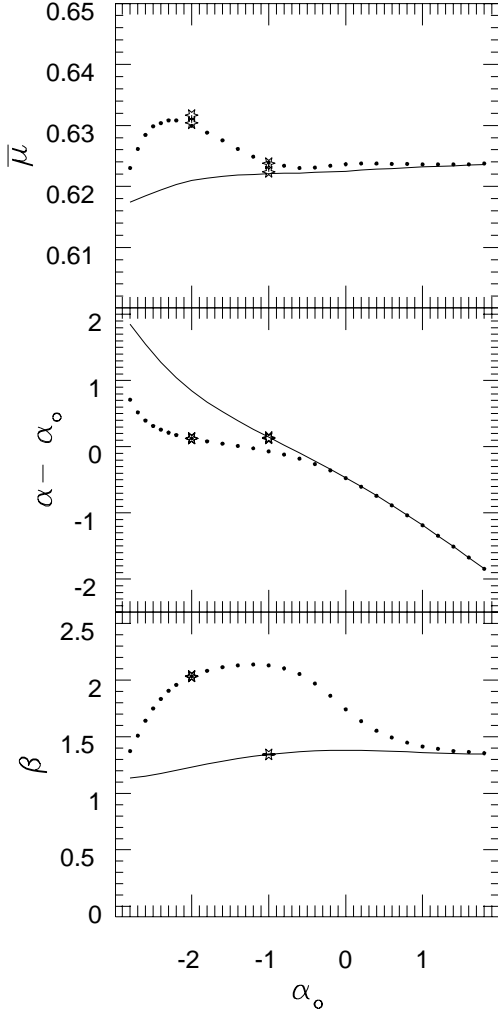


Figure 9. Systematic shift (bias) in the inferred parameters relative to their ‘real’ values as a function of the real α_o . It is assumed that the real halo is of the ‘CS’ type, while the singular isothermal sphere (SIS) is used in the inference of $\bar{\mu}$, α and β . For the dotted lines $\beta_o = 2$, while for the solid lines $\beta_o = 1$. In all cases $(\bar{\mu})_o = 0.4$. The curves were obtained by maximisation of expression (25). The stars indicate the results of Monte-Carlo simulations. The vertical segments bordered by stars in the plot of $\bar{\mu}$ give the 1σ error for the Monte-Carlo simulations.

(solid curve) and $\beta_o = 2$ (dotted curve). These results were obtained by maximising expression (25) for $\varepsilon(T) = \text{const.}$

We first notice the upward shift in the inferred average mass $\bar{\mu}$ by about 60%. The inferred mass scales as $\mu \sim \sigma^2 / \langle x(1-x) \rangle$, where σ is the typical velocity dispersion in the halo and $\langle x(1-x) \rangle$ denotes the average of the quantity over the differential event rate. By using the SIS instead of the ‘right’ CS halo model, we gain a factor of 2–3 due to the increased σ (see Fig. 1), while the mass estimate is reduced due to the larger $\langle x(1-x) \rangle$ (the SIS halo is more extended). The net result is a shift in $\bar{\mu}$ that depends only weakly on α_o and β_o . [The segments bordered by stars show results of Monte-Carlo simulations (10000 events) up to their statistical errors obtained from 400 simulations. The

agreement with the results obtained by minimising (25) is good but not perfect. See Appendix for a brief discussion of the limitations of the method based on equation (25).]

We also notice that for $-2 \lesssim \alpha_o \lesssim 0$ both α and β are relatively weakly affected by the uncertainties of the halo model. This may be expected on the basis of our discussion (see the last Section) of the ‘plateau’ in $P(T)$ for values of α_o near -1.5 . The presence of the ‘plateau’ is independent of the halo model; it is a robust property carried over from $P_o(T)$ to $P(T)$. (Our results for various values of the ‘true’ halo parameters, γ , σ_o , σ_+ , r_o and l , indicate that α and β are generally insensitive to the halo model uncertainties in the above range of α .)

By contrast, for $\alpha_o \gtrsim 0.5$ the shift is significant. In this range of α_o , $\Psi(\mathbf{c}, \mathbf{c}_o)$ as a function of α and β is very flat and insensitive to shifts in the two parameters. Due to this circumstance, even a slight ‘tilt’ to the function $\Psi(\mathbf{c}, \mathbf{c}_o)$ due to a switch to another halo model is likely to lead to a large shift in the position of the function’s maximum in the (α, β) plane. This is closely related to the basic reasons for large statistical errors for $\alpha_o \gtrsim 0.5$ that we discussed in the last section. From the point of view of the inference of α and β , the bias due to the uncertainty of the halo model would in this case only compound already very large statistical errors. The same holds for large negative values of α (< -2.5).

In addition to the effect on the mass function determination, MHO distribution and kinematics uncertainties will bear on the determination of the density and total mass in the massive objects’ halo. If $\varepsilon = \text{const.}$ the two integrations in the total rate (22) can be performed in the reversed order

$$\begin{aligned} \int_0^\infty dT T^{2(\alpha+1)} \int_{\mu_o \frac{10^{-\beta/2}}{T^2}}^{\mu_o \frac{10^{\beta/2}}{T^2}} dy y^\alpha F(y) \\ = \int_0^\infty dy y^\alpha F(y) \int_{\sqrt{\mu_o/y} 10^{-\beta/4}}^{\sqrt{\mu_o/y} 10^{\beta/4}} dT T^{2(\alpha+1)} \\ = \frac{1}{2} \mu_o^{\alpha+3/2} C_\beta(\alpha+1/2) \int_0^\infty F(y) y^{-3/2} dy, \end{aligned} \quad (26)$$

and the total rate takes on the form

$$\Gamma = K \rho_o \frac{1}{\bar{\mu}} \Xi(\alpha, \beta) \int_0^\infty F(y) y^{-3/2} dy, \quad (27)$$

where K is a constant independent of either the halo model or the MHO mass function and

$$\Xi(\alpha, \beta) \equiv \frac{C_\beta(\alpha+1/2)}{\sqrt{C_\beta(\alpha)C_\beta(\alpha+1)}}. \quad (28)$$

Obviously [see equation (17)], $F(y)$ depends only on the halo model but not on the parameters of the mass function. It also turns out that the equality $\Xi(\alpha, \beta)/\Xi(\alpha_o, \beta_o) = 1$ [$\alpha(\alpha_o, \beta_o)$ and $\beta(\alpha_o, \beta_o)$ are again the best fits obtained with the ‘false’ halo model] is satisfied with better than 1% accuracy for the range of α and β discussed in this paper. Since the inferred $\bar{\mu}$, shown in Fig. 9, depends only very weakly on α and β it follows that the ratio $(\rho_o)_{\text{biased}}/(\rho_o)_{\text{real}}$ is practically independent of α and β .

In the case discussed in this section so far, where the CS halo is chosen as the ‘real’ one and the SIS as the halo model used in the inference of the mass function, we obtain $(\rho_o)_{\text{biased}}/(\rho_o)_{\text{real}} \simeq 0.5$. Although the inferred value

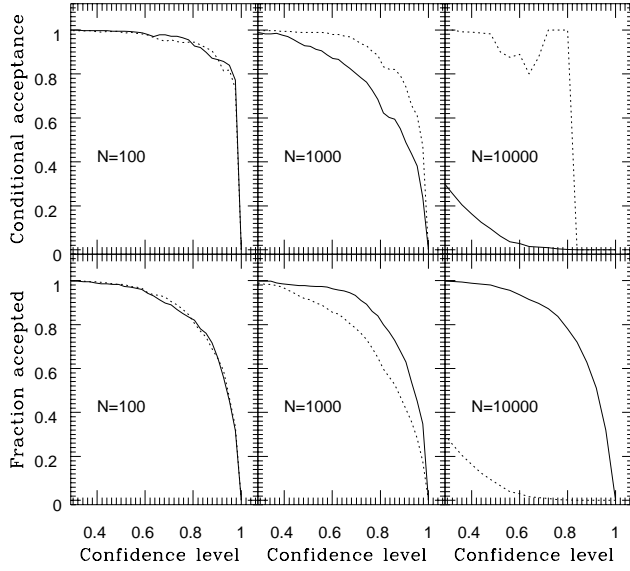


Figure 10. The acceptable fraction (bottom) of best fit curves $P(T)$ based on the ‘real’ CS halo (solid line) and ‘false’ SIS halo (dotted line) as functions of Kolmogorov-Smirnov confidence levels for $N = 100$, $N = 1000$ and $N = 10000$ detected events. The ‘real’ mass function is $\bar{\mu} = 0.4$, $\alpha = -2$ and $\beta = 2$. In the upper panels the solid lines give the ‘probability’ that *if* a CS-based best fit is accepted at the given confidence level, the SIS-based best fit will also pass the Kolmogorov-Smirnov test. The dotted lines show the probability of acceptance of a CS-based fit given that the SIS-based fit is acceptable.

of the local MHO halo density ρ_o is only half the actual one, the much slower fall-off of the SIS density at larger distances leads to the inferred total halo mass, $M_{\text{tot}} = 4\pi \int_{R_\odot}^{R_{\text{LMC}}} \rho_o(r/R_\odot)^{-\gamma} r^2 dr$, between the Sun and the LMC being about twice the actual amount.

Since both the isothermal sphere and the ‘concentrated’ sphere can be viewed as plausible models of the massive objects’ halo, the parameter shifts evaluated so far in this section provide an estimate of the magnitude of error due to halo structure uncertainty. As we have stated above, due to the difficulty of distinguishing among different halo structures on the basis of event duration measurements only, it would appear unlikely that these (systematic) errors should be possible to eliminate.

On the other hand, we have noticed in the early part of this section that for α in the range most conducive to mass function parameter inference ($\alpha \sim -1.5$), there is a residual difference between the differential event rate based on one halo model and its best match based on a different halo structure (upper panel of Fig. 8). Can this difference be exploited in a realistic statistical inference in order to reduce the effect of the halo structure uncertainty? Specifically, with how many detected events do we need to sample the differential rate so that the small difference can be recognised?

In order to answer this question we perform a number (400) of Monte-Carlo simulations of the mass function parameters’ statistical inference. Again, we assume that the

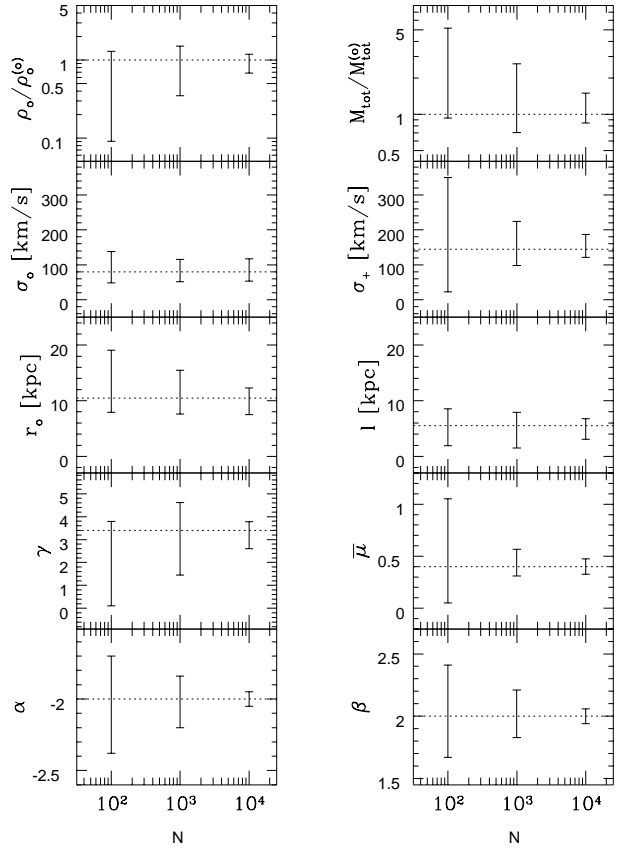


Figure 11. ‘ 1σ ’ confidence intervals (obtained by simulations where *all* eight parameters are varied in the maximum likelihood method) as functions of the number of detected events N . The dotted lines give the values of the ‘real’ parameters.

‘real’ halo is CS, $\bar{\mu}_o = 0.4$, $\alpha = -2$, and $\beta = 2$, generate a given number of events ($N = 100, 1000$ or 10000) and obtain maximum likelihood fits based in turns on the CS and the (‘false’) SIS halo. In Fig. 10 we show the results of the Kolmogorov-Smirnov test of acceptability of the maximum likelihood fits (based on the two different halos) as models for the observed data.

At $N = 100$ it makes virtually no difference which halo model is used as a basis for statistical inference: the small discrepancy between the two event rate curves observed in Fig. 8 is completely swamped by the statistical noise. On the other hand, for $N = 1000$ the difference starts to be significant, although the probability of confusion between the two halos in any single data realisation is still high. At $N = 10000$ the ambiguity is completely resolved. Obviously, it is at about $N = 1000$ that we may first start discerning the halo structure effects and thus hope to be able to reduce the (halo model-induced) errors in the mass function parameters estimated earlier in this section.

This conclusion is borne out by Monte-Carlo simulations where all eight parameters ($\gamma, \sigma_o, \sigma_+, r_o, l, \bar{\mu}, \alpha$ and β) are varied with a uniform prior to obtain maximum-likelihood fits to events distributed according to the differential event rate whose parameters are indicated by the dotted lines in Fig. 11. The vertical bars show ‘ 1σ ’ intervals for inferred values of the parameters. [The inferred ρ_o and M_{tot}

are simply read out from the event rate (10) given a fixed event number of events and observation time without allowing for the inevitable Poisson count noise.]

As we concluded earlier in this section, for $\alpha_o = -2$ the effects of the halo uncertainty on α and β are rather weak and these parameters are obtained with a good accuracy from between 100 and 1000 events. The halo model uncertainty adds little to the errors estimated in the last section. On the other hand, the error in $\bar{\mu}$ falls below the level estimated above in this section only at $N \sim 1000$. Notice that at $N = 10000$ the error is larger by a factor of about 10 than the value obtained with a fixed halo model (see Fig. 5).

The improvement at $N \approx 1000$ is not necessarily reflected in an accurate knowledge of the structure of the halo: for instance, r_o and l , and thus the velocity profile, are not accurately determined even for the largest N 's shown in Fig. 11. It is rather that for N near 1000 the halo is constrained just enough to allow a more reliable mass function inference; the small gap between the two curves of the upper panel of Fig. 8 can thus be much reduced with a rather broad range of best-fit halo models.

Probably the most important quantities characterising the halo, its local density ρ_o and total mass between the Sun and LMC, M_{tot} (themselves functions of the above eight parameters and the observed event rate) clearly gain in accuracy with increasing N (see the two top panels of Fig. 11). However, it should be pointed out that only at around $N = 10000$ is the error due to halo structure uncertainty reduced to roughly the level of the simple Poisson count fluctuation $1/\sqrt{6} \approx 40\%$ associated with the total number of (reliable) LMC events detected by the time of this writing.

Acknowledgements

This research was generously supported by Danmarks Grundforskningsfond through its establishment of the Theoretical Astrophysics Center.

REFERENCES

- Abramowitz, M. & Stegun, I.A., 1972, Handbook of Mathematical Functions. National Bureau of Standards, Washington DC
- Alcock, C. *et al.* 1996, astro-ph/9606165
- Aubourg, E. *et al.* 1993, Nature 365, 623
- Bahcall, J., Schmidt, M. & Soneira, R.M., 1983, Ap. J. 265, 730
- Binney, J. & Tremaine, S., 1987, Galactic Dynamics. Princeton Univ. Press, Princeton
- Caldwell, J.A.R. & Ostriker, J.P., 1981, Ap. J. 251, 61
- Cramer, H., 1946, Mathematical Methods of Statistics. Princeton Univ. Press, Princeton
- De Rújula, A., Jetzer, Ph. & Massó, E., 1991, MNRAS 250, 348
- De Rújula, A., Giudice, G.F., Mollerach, S. & Roulet, E., 1995, MNRAS 275, 545
- Giudice, G.F., Mollerach, S. & Roulet, E., 1994, Phys. Rev. D50, 2406
- Gould, A., 1992, Ap. J. 392, 442
- Gould, A., 1994, Ap. J. 421, L75
- Gould, A., 1995a, Ap. J. 440, 510
- Gould, A., 1995b, Ap. J. 441, L21
- Griest, K., 1991, Ap. J. 366, 412
- Jetzer, P. & Massó, E., 1994, Phys. Lett. B 323, 347
- Jetzer, P., 1996, astro-ph/9609016

- Mao, S. & Paczynski, B., 1996, astro-ph/9604002
- Paczynski, B., 1986, Ap. J. 304, 1
- Paczynski, B., 1996, Gravitational Microlensing in the Local Group, Ann. Rev. Astro. and Astrophys., in press; astro-ph/9604011
- Refsdal, S., 1966, MNRAS 134, 315
- Rohlf, K & Kreitschmann, J., 1988, Astr. & Astrophys. 201, 51
- Roulet, E. & Mollerach, S., 1996, Microlensing, Phys. Rep., in press; astro-ph/9603119
- Sommer-Larsen, J., Flynn C. & Christensen, P.R., 1994, MNRAS, 271, 94
- Sommer-Larsen, J. & Markovic, D., 1997, in preparation

Appendix: Bias, error and the maximum likelihood method

In this appendix we summarise some known mathematical results pertinent to the problem of estimating parameters of a probability distribution, given a set of measurements [see also (Cramer 1946)].

Suppose we have a set of N measurement results $\mathbf{x} \equiv \{x_1, x_2, \dots, x_N\}$. Suppose also that the measurements are distributed according to the probability distribution $f(x|\mathbf{c})$ ($\int f dx = 1$), where \mathbf{c} denotes a set of p parameters which are *a priori* unknown. *Estimator* $\hat{\mathbf{c}}(\mathbf{x})$ is then a function of the measurement results that can serve as a reasonable estimate of the values of the underlying parameters \mathbf{c} .

Any statistical inference is, in principle, subject to error and bias in the inferred parameters. For each parameter c_μ the variance of estimation is defined as

$$\sigma_{c_\mu}^2 \equiv E(\hat{c}_\mu^2) - E^2(\hat{c}_\mu), \quad (\text{A1})$$

where E denotes the expectation value of an ensemble whose each member consists of N measurements under the same conditions; \hat{c}_μ are the values of parameters estimated from the n measurements in a member of the ensemble. On the other hand, the bias

$$b_\mu \equiv E(\delta c_\mu) = E(\hat{c}_\mu) - c_\mu \quad (\text{A2})$$

is the systematic departure of estimated parameters from the ‘true’ parameters \mathbf{c} .

Given the dependence of bias on the the underlying parameters, the errors of estimation are bounded from below by the Cramer (also known as Frechet-Cramer-Rao) limit, as we derive in the following.

Denoting $F(\mathbf{x}|\mathbf{c}) \equiv f(x_1|\mathbf{c})f(x_2|\mathbf{c}) \cdots f(x_N|\mathbf{c})$, the definition of bias (A2) can be rewritten as

$$\int \hat{c}_\mu(\mathbf{x}) F(\mathbf{x}|\mathbf{c}) d^n \mathbf{x} = c_\mu + b_\mu. \quad (\text{A3})$$

Differentiating the above equation with respect to parameter c_ν we obtain

$$E(\hat{c}_\mu l_{,\nu}) = E[(\hat{c}_\mu - E(\hat{c}_\mu)) l_{,\nu}] = \delta_{\mu\nu} + b_{\mu,\nu}, \quad (\text{A4})$$

where we have used

$$l(\mathbf{x}, \mathbf{c}) \equiv \ln F(\mathbf{x}|\mathbf{c}), \quad (\text{A5})$$

and the fact that

$$E(l_{,\mu}) = N \int [\ln f(x|\mathbf{c})]_{,\mu} f(x|\mathbf{c}) dx = 0, \quad (\text{A6})$$

due to the normalisation of f . Convolving the matrix equation (A4) with arbitrary p -dimensional vectors u_μ and v_ν and using the Schwartz inequality, we obtain

$$V_{\mu\nu} u_\mu u_\nu I_{\rho\sigma}^{(n)} v_\rho v_\sigma \geq (u_\mu v_\mu + b_{\mu,\nu} u_\mu v_\nu)^2, \quad (\text{A7})$$

where we have used Einstein's convention of summation over repeated indices and defined the variance matrix

$$V_{\mu\nu} \equiv E[(\hat{c}_\mu - E(\hat{c}_\mu))(\hat{c}_\nu - E(\hat{c}_\nu))], \quad (\text{A8})$$

and the information matrix

$$\begin{aligned} I_{\mu\nu}^{(n)} &= E(l_{,\mu} l_{,\nu}) = N I_{\mu\nu} \\ &= N \int (\ln f(x|\mathbf{c}))_{,\mu} (\ln f(x|\mathbf{c}))_{,\nu} f(x|\mathbf{c}) dx. \end{aligned} \quad (\text{A9})$$

It is convenient at this point to simplify notation by introducing Dirac-style bra/ket notation. Thus, $|u\rangle$ denotes the column u_μ while $\langle u|$ denotes the corresponding row. The equation (A7) can now be rewritten as

$$\langle u|V|u\rangle \geq \frac{(\langle u|v\rangle + \langle u|B|v\rangle)^2}{\langle v|I|v\rangle}, \quad (\text{A10})$$

where $B_{\mu\nu} \equiv b_{\mu,\nu}$. Since $|v\rangle$ is arbitrary, we can find the maximum of the right-hand side in the above equation (for a given $|u\rangle$) if we require that the first derivative with respect to $|v\rangle$ be zero. This condition leads to

$$\langle u|(1+B) \left(\mathbf{1} - \frac{|v\rangle\langle v|}{\langle v|I|v\rangle} I \right) = 0. \quad (\text{A11})$$

It is straightforward to see that the vector satisfying condition (A11) is

$$|v\rangle = I^{-1} (1+B^T) |u\rangle, \quad (\text{A12})$$

which by substitution in equation (A10) gives the Cramer inequality

$$\langle u|V|u\rangle \geq \langle u|(1+B)I^{-1}(1+B^T)|u\rangle, \quad (\text{A13})$$

where $|u\rangle$ is an arbitrary p -dimensional vector.

In general, the Cramer inequality is only of limited utility: the actual estimator we are using may have variance that far exceeds the Cramer limit. In addition, it may be difficult to determine the bias, which is needed to compute the Cramer limit in the first place. However, as we show below, the method of maximum likelihood is asymptotically (for N large enough) unbiased and approaches the Cramer limit.

In the maximum likelihood method one adopts as estimates $\hat{\mathbf{c}}$ of the parameters determining distribution $f(x|\mathbf{c})$ those values of the parameters that yield the maximum of $l(\mathbf{x}|\mathbf{c})$ [see equation (A5)] given a set \mathbf{x} of N measurements. Expanding the maximum likelihood condition in the vicinity of the true values of the parameters \mathbf{c} , $0 = l_{,\mu}(\hat{\mathbf{c}}) = l_{,\mu}(\mathbf{c}) + (\hat{c}_\nu - c_\nu) l_{,\mu\nu}(\mathbf{c})$ we obtain the 'shift' from the true parameters

$$\hat{c}_\mu - c_\mu = -[l_{,\mu\nu}]^{-1} l_{,\nu}, \quad (\text{A14})$$

where $[l_{,\mu\nu}]^{-1}$ denotes the inverse matrix of $[l_{,\mu\nu}]$. For n large enough, $[l_{,\mu\nu}]^{-1}$ can be approximated by its ensemble average

$$[l_{,\mu\nu}]^{-1} \approx E\{[l_{,\mu\nu}]^{-1}\} \approx [E(l_{,\mu\nu})]^{-1} = [I_{\mu\nu}^{(N)}(\mathbf{c})]^{-1}, \quad (\text{A15})$$

where we have substituted $E(l_{,\mu\nu}) = -E(l_{,\mu} l_{,\nu})$, which is a straightforward consequence of the normalisation of f . Due

to equation (A6) the bias asymptotically vanishes, while the variance (A8) approaches the Cramer limit

$$\begin{aligned} V_{\mu\nu} &= E\{[l_{,\mu\rho}]^{-1} [l_{,\nu\sigma}]^{-1} l_{\rho} l_{\sigma}\} \\ &\approx [I_{\mu\rho}^{(N)}(\mathbf{c})]^{-1} [I_{\nu\sigma}^{(N)}(\mathbf{c})]^{-1} E[l_{\rho} l_{\sigma}] \\ &\approx [I_{\mu\nu}^{(N)}(\mathbf{c})]^{-1}, \end{aligned} \quad (\text{A16})$$

where, in the last equality we used equation (A9). We denote the corresponding 'Cramer' deviation limit as $\Delta_{cc_\mu} \equiv (nV_{\mu\mu})^{1/2}$.

In the above outline of the maximum likelihood method we assumed that all uncertainty regarding the underlying distribution function $f(\mathbf{x}|\mathbf{c})$ stems from the uncertainty of the values of a well defined, finite set of parameters, while the functional dependence $f(\mathbf{x}|\mathbf{c})$ is known. In the more general case, the functional dependence is not known accurately. We can then ask the following question: if we happen to be using a 'wrong' functional dependence $f(\mathbf{x}|\mathbf{c}) = f_o(\mathbf{x}|\mathbf{c}) + \delta f(\mathbf{x}|\mathbf{c})$ instead of the correct function $f_o(\mathbf{x}|\mathbf{c})$, what will be the bias (A2), i.e., the average departure from the true parameters. Obviously, in this case the bias need not be asymptotically zero.

More specifically, the maximum likelihood method looks for the maximum of $l(x|\hat{\mathbf{c}}) \equiv \sum_{i=0}^N \ln f(x_i|\hat{\mathbf{c}})$, where \mathbf{x} are results of measurements distributed according to the true function f_o , i.e., it seeks the values $\hat{\mathbf{c}}$ for which $l(x|\hat{\mathbf{c}})_{,\mu} = 0$. A reasonable approach to estimating the average value of $\hat{\mathbf{c}}$ that this method would give for large n , may be to look for those values of $\hat{\mathbf{c}}$ that maximize

$$\Psi(\hat{\mathbf{c}}, \mathbf{c}) = \int f_o(x|\mathbf{c}) \ln f(x|\hat{\mathbf{c}}) dx. \quad (\text{A17})$$

In other words, the requirement is

$$\partial\Psi(\hat{\mathbf{c}}, \mathbf{c})/\partial\hat{c}_\mu = 0. \quad (\text{A18})$$

Note that if $f = f_o$, this condition simply implies $\hat{\mathbf{c}} = \mathbf{c}$.

Unfortunately, this prescription finds the maximum of the average of $l(\mathbf{x}|\hat{\mathbf{c}})$ which quite obviously need not be the same as the required average of those $\hat{\mathbf{c}}$ that maximize $l(\mathbf{x}|\hat{\mathbf{c}})$ for different measurement sets \mathbf{x} . Still, for small enough δf the two quantities are very close to each other. Indeed, in this case

$$\begin{aligned} l(x|\hat{\mathbf{c}}) &= \sum_{i=0}^N \ln[f_o(x_i|\hat{\mathbf{c}}) + \delta f(x_i|\hat{\mathbf{c}})] \\ &\approx \sum_{i=0}^N (\ln f_o + \delta f/f_o). \end{aligned} \quad (\text{A19})$$

From equation (A14) we then obtain

$$b_\mu = E(\hat{c}_\mu - c_\mu) \approx [I_{\mu\nu}]^{-1} E\left(\frac{1}{f_o} \delta f_{,\nu} - \frac{\delta f}{f_o^2} f_{o,\nu}\right), \quad (\text{A20})$$

where we have kept only terms linear in δf and used the fact that $E(l_o) = 0$. On the other hand, the condition $\partial\Psi(\hat{\mathbf{c}}, \mathbf{c})/\partial\hat{c}_\mu = 0$ gives

$$\begin{aligned} 0 &= \int f_o dx(x|\mathbf{c}) \frac{\partial}{\partial\hat{c}_\mu} \left[\ln f_o(x|\hat{\mathbf{c}}) + \frac{\delta f}{f_o} \right] \\ &\approx \int f_o dx \left[(\ln f_o(x|\mathbf{c}))_{,\mu} + (\hat{c}_\nu - c_\nu) (\ln f_o(x|\mathbf{c}))_{,\mu\nu} \right. \\ &\quad \left. + \frac{1}{f_o} \delta f_{,\nu} - \frac{\delta f}{f_o^2} f_{o,\nu} \right], \end{aligned} \quad (\text{A21})$$

which in the limit of large n leads to equation (A20).

Although, strictly speaking, condition (A18) holds only for small δf , its cautious application can yield a reasonable estimate of bias even away from this strict limit.